Anisotropic Spin-Acoustic Resonance in Silicon Carbide at Room Temperature

A. Hernández-Mínguez,[1,*] A. V. Poshakinskiy,[2] M. Hollenbach,[3,4] P. V. Santos,[1] and G. V. Astakhov[3]

[1]*Paul-Drude-Institut für Festkörperelektronik, Leibniz-Institut im Forschungsverbund Berlin e.V., Hausvogteiplatz 5-7, 10117 Berlin, Germany*

[2]*Ioffe Physical-Technical Institute, Russian Academy of Sciences, 194021 St. Petersburg, Russia*

[3]*Helmholtz-Zentrum Dresden-Rossendorf, Institute of Ion Beam Physics and Materials Research, Bautzner Landstrasse 400, 01328 Dresden, Germany*

[4]*Technische Universität Dresden, 01062 Dresden, Germany*

(Received 2 May 2020; revised 30 June 2020; accepted 6 August 2020; published 3 September 2020)

We report on acoustically driven spin resonances in atomic-scale centers in silicon carbide at room temperature. Specifically, we use a surface acoustic wave cavity to selectively address spin transitions with magnetic quantum number differences of ± 1 and ± 2 in the absence of external microwave electromagnetic fields. These spin-acoustic resonances reveal a nontrivial dependence on the static magnetic field orientation, which is attributed to the intrinsic symmetry of the acoustic fields combined with the peculiar properties of a half-integer spin system. We develop a microscopic model of the spin-acoustic interaction, which describes our experimental data without fitting parameters. Furthermore, we predict that traveling surface waves lead to a chiral spin-acoustic resonance that changes upon magnetic field inversion. These results establish silicon carbide as a highly promising hybrid platform for on-chip spin-optomechanical quantum control enabling engineered interactions at room temperature.

DOI: 10.1103/PhysRevLett.125.107702

Hybrid spin-mechanical systems are considered as a promising platform for the implementation of universal quantum transducers [1] and ultrasensitive quantum sensors [2]. Spin states can be coupled by the strain fields of phonons and mechanical vibrations. Coherent sensing of mechanical resonators [3], acoustic control of single spins [4], and electromechanical stabilization of spin color centers [5] based on spin-optomechanical coupling have been demonstrated. Similarly to a magnetic field, the application of a static strain field leads to a shift of the spin levels, while a resonantly oscillating strain field induces interlevel spin transitions. Their selection rules are imprinted by the crystal symmetry or device geometry, which provide a high degree of flexibility for on-chip coherent spin manipulation [6–8] and may support chiral spin-phonon coupling [9].

Most of the systems coupling atomic-scale spins to vibrations studied so far are based on color centers in diamond [3–5,10–14]. Two characteristics of silicon carbide (SiC) make it a natural material choice for hybrid spin optomechanics. As diamond, SiC hosts highly coherent optically active spin centers such as negatively charged silicon vacancies (V_{Si}) [15] and divacancies (VV) [16]. In addition, SiC is already used in commercial nanoelectromechanical systems with robust performance and ultrahigh sensitivity to vibrations [17]. Recently, the mechanical tuning [18] and acoustic coherent control [19] of the VV spin $S = 1$ centers in SiC have been demonstrated at cryogenic temperatures. However, symmetry-dependent spin-acoustic interactions are still largely unexplored, and SiC-based hybrid spin-mechanical systems under ambient conditions remain elusive.

In this Letter, we demonstrate room-temperature spin-acoustic resonance (SAR) in 4H-SiC. We exploit the intrinsic properties of the half-integer spin $S = 3/2$ system [20], the so-called V_{Si} qudit [21], to realize full control of the spin states using high-frequency vibrations. This is fulfilled by acoustically coupling spin sublevels with magnetic quantum numbers (m_S) differing by both $\Delta m_S = \pm 1$ and $\Delta m_S = \pm 2$. The previous SAR studies were mostly restricted to $S = 1$ atomic-scale spins [3,5,10–14,18,19], which usually require the application of microwave electromagnetic fields for the optical readout. Very recently, microwave-free SAR resonance has been demonstrated in a spin $S = 1/2$ system with strong spin-orbit coupling at cryogenic temperature [4]. We show that the spin $S = 3/2$ system enables all-optical readout without external microwave electromagnetic fields even at room temperature.

The mechanical vibrations are applied via a surface acoustic wave (SAW) resonator patterned on the surface of a 4H-SiC wafer perpendicular to the c hexagonal axis (see Fig. 1). The superposition of axial and shear strain components with different amplitudes and phases makes the SARs dependent on the quantization direction of the spin states relative to the SAW propagation direction. Here, this anisotropy manifests itself as a complex angular dependence of the $\Delta m_S = \pm 1$ and $\Delta m_S = \pm 2$ transitions

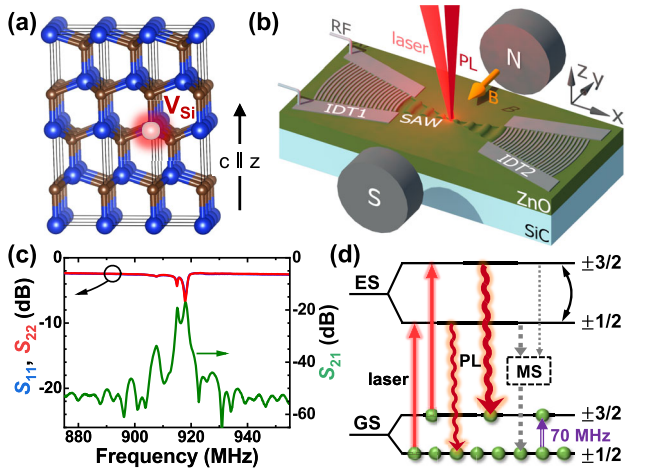

FIG. 1. Schematic presentation of (a) the 4H-SiC lattice with one V_{Si} defect and (b) the acoustic device. Focusing IDTs excite and detect SAWs propagating on the ZnO-coated SiC. The sample is placed between the poles of an electromagnet for the application of a magnetic field $\boldsymbol{B}$ along the sample surface. (c) rf scattering parameters for IDT1 and IDT2. S_{11} and S_{22} correspond to the rf power reflection coefficients of IDT1 and IDT2, respectively, and S_{21} to the power transmission coefficient. (d) Optical pumping cycle and readout principle of the V_{Si} spin. The double vertical arrow indicates the spin resonance transition at 70 MHz in zero magnetic field (see Supplemental Material (SM) [27]).

on the orientation of the external magnetic field $\boldsymbol{B} = (B_x, B_y, 0)$ oriented along the SiC surface [i.e., with $B_z = 0$, cf. Fig. 1(b)]. We develop a model for spin-3/2 SARs using an effective spin-strain coupling Hamiltonian [2,22], which can describe our nontrivial observations. The selective excitation of transitions with $\Delta m_S = \pm 1$ and $\Delta m_S = \pm 2$ as well as the anisotropic behavior with magnetic field orientation demonstrated here provides extra degrees of freedom for the control of interactions in atomic-scale spin systems.

Figure 1(a) displays the 4H-SiC lattice with a single V_{Si} center [23]. These centers are created in a semi-insulating 4H-SiC substrate by proton irradiation [24]. Figure 2(d) shows the calculated depth distribution of the V_{Si} centers, which has a mean depth of 250 nm below the SiC surface [25]. As shown in the SM [27], the observed zero-field spin splitting of 70 MHz is characteristic of the V2 centers [28–31]. Figure 1(b) displays a schematic representation of our acoustic SAW resonator [27]. It consists of a pair of focusing interdigital transducers (IDTs) for the excitation and detection of SAWs with a wavelength $\lambda_{SAW} = 6\ \mu$m patterned on a SiC wafer coated with a piezoelectric ZnO film. Figure 1(c) displays the rf scattering parameters of the IDTs measured with a vector network analyzer. They show a series of sharp dips within the resonance band of the IDT at a frequency $f_{SAW} \approx 916$ MHz that correspond to the excitation of the Rayleigh SAW modes of the resonator [32].

Figure 1(d) displays a simplified energy diagram of the V2 V_{Si} center [23,33] together with the optical pumping and readout scheme [34]. The V_{Si} center has spin 3/2, which is split in zero magnetic field into two Kramers doublets in the SiC crystal field. The zero-field splitting between the $m_S = \pm 1/2$ and $m_S = \pm 3/2$ doublets in the ground state (GS) is equal to 70 MHz, with the spin quantized along the c axis. Optical excitation into the excited state, followed by spin-dependent recombination via the metastable state, leads to a preferential population of the $m_S = \pm 1/2$ spin sublevels in the ground state, as indicated by the green dots in Fig. 1(d). For the optical excitation along the c axis (as in our experiments), no dependence on the excitation polarization is observed at room temperature. As the photoluminescence intensity is stronger for optical transitions between the $m_S = \pm 3/2$ states, it becomes sensitive to the resonant spin transitions between the $m_S = \pm 1/2$ and $m_S = \pm 3/2$ GS sublevels (see SM [27]) [31].

The optically detected SAR experiments are performed in a confocal microphotoluminescence setup in which the sample is excited by a 780-nm-wavelength laser focused onto a spot size of 10 μm at the center of the SAW resonator. The GS spin transition frequencies are tuned to the SAW resonance frequency by applying the in-plane magnetic field $\boldsymbol{B}$ [27]. To describe the spin-acoustic interaction of the V_{Si} center in the presence of $\boldsymbol{B}$, we consider an effective spin-3/2 Hamiltonian

$$\mathcal{H} = \mathcal{H}_B + \mathcal{H}_{\rm def}, \quad \text{with} \tag{1}$$

$$\mathcal{H}_B = g\mu_B \boldsymbol{S}\cdot\boldsymbol{B} + D\left(S_z^2 - \frac{5}{4}\right). \tag{2}$$

Here, $\boldsymbol{S}=(S_x, S_y, S_z)$ is the spin-3/2 operator, μ_B the Bohr magneton, $g \approx 2$ the in-plane g factor, and $D = 35$ MHz the zero-field splitting constant. $\mathcal{H}_B$ describes the Zeeman splitting. For $\boldsymbol{B} = 0$, this Hamiltonian yields the GS eigenstates displayed in Fig. 1(d). As discussed below, $\mathcal{H}_{\rm def}$ describes the coupling between the V_{Si} spin and elastic deformations [2,22].

Figure 2(a) shows the Zeeman shift of the GS spin sublevels calculated from $\mathcal{H}_B$. In what follows, we consider magnetic fields much larger than the GS zero-field splitting $2D/g\mu_B \sim 2.5$ mT. In this case, the spin quantization axis aligns along the $\boldsymbol{B}$ direction and the spin sublevels shift linearly with the magnetic field. The mixing of the states quantized along $\boldsymbol{B}$ is on the order of $D/(g\mu_B B)$ and can be neglected. We note that for in-plane magnetic fields, the states with spin projection on magnetic field direction $m_S = \pm 3/2$ are preferentially populated under optical pumping (as indicated by the green dots). In contrast to the $\boldsymbol{B} = 0$ case illustrated in Fig. 1(d), the photoluminescence is now stronger for transitions between the excited state and GS involving the $m_S = \pm 1/2$ states (see the light bulbs next to each energy level).

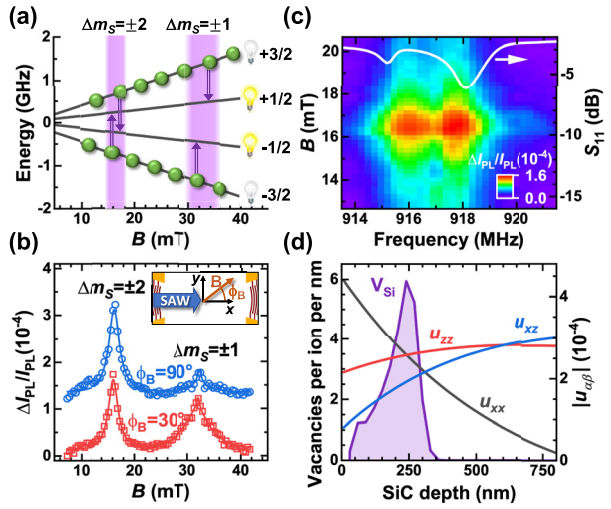

FIG. 2. (a) Evolution of the V_{Si} GS spin levels under an in-plane magnetic field $\boldsymbol{B}\perp c$. The vertical double arrows indicate the resonant spin transitions at 916 MHz induced by the SAW. (b) The SAR signal as a function of the magnetic field strength. The data are measured for two magnetic field angles (ϕ_B) with respect to the SAW propagation direction (see inset). The solid curves are fits to a multipeak Lorentzian function. The data are vertically shifted for clarity. (c) Two-dimensional color map of the $\Delta m_S = \pm 2$ spin transition strength as a function of B and the rf frequency applied to the IDT. The line shows the power reflection coefficient S_{11} of the IDT. (d) Simulated depth profiles for the distribution of vacancies after irradiation (which is proportional to the density of V_{Si} centers) as well as of the u_{xx}, u_{zz}, and u_{xz} strain amplitudes.

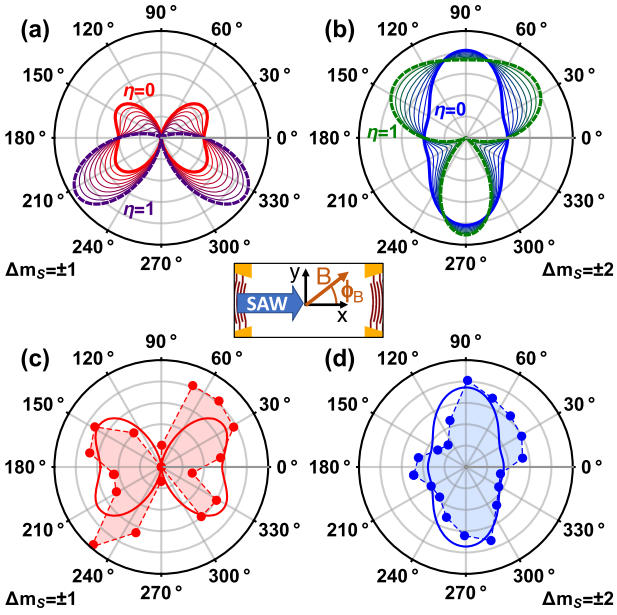

FIG. 3. (a),(b) Dependence of the $\Delta m_S = \pm 1$ and $\Delta m_S = \pm 2$ transition intensities on the angle ϕ_B between the in-plane magnetic field and the SAW propagation direction (see inset) calculated for a standing wave ($\eta = 0$, thick thick lines), a traveling wave ($\eta = 1$, dashed thick lines), and intermediate values of η. The strain components used are $\langle u_{xx}^2\rangle = 8.1\times10^{-8}$, $\langle u_{zz}^2\rangle = 6.3\times10^{-8}$, $\langle u_{xz}'^2\rangle = 3.2\times10^{-8}$, $\langle u_{xx}u_{zz}\rangle = 7.0\times10^{-8}$, $\langle u_{xx}u_{xz}''\rangle = 4.8\times10^{-8}$, and $\langle u_{xz}''u_{zz}\rangle = 4.5\times10^{-8}$ as obtained from the distributions of Fig. 2(d). (c),(d) Angular dependencies of the $\Delta m_S = \pm 1$ and $\Delta m_S = \pm 2$ transition amplitudes as a function of ϕ_B. Circles present the experimental data, the dashed lines are guides to the eye. The thick lines show the calculation after Eq. (4) with $\eta = 0$.

The optically detected SAR as a function of B is presented in Fig. 2(b). We observe two resonances at $B = 16.7$ mT and $B = 33.3$ mT, which are ascribed to the acoustically driven $\Delta m_S = \pm 2$ and $\Delta m_S = \pm 1$ spin transitions, respectively. They agree well with the magnetic field strengths calculated from Eq. (1) for the resonance frequency $f_{\mathrm{SAW}} = 916$ MHz [cf. double vertical arrows in Fig. 2(a)]. Both resonances are well fitted by a Lorentzian function [solid curves in Fig. 2(b)] with an FWHM of 2.2 mT and 6.0 mT, respectively. Due to the zero-field splitting [cf. Eq. (2)], these resonances are actually doublets. With the zero-field spin splitting of 70 MHz, they should be split by approximately 1 mT and 2 mT for the $\Delta m_S = \pm 2$ and $\Delta m_S = \pm 1$ spin transitions, respectively. These splittings are not resolved due to a relatively large broadening partially caused by a reduction of the spin coherence in proton-irradiated samples with high irradiation fluences [35].

A remarkable property of the SAR interaction illustrated in Fig. 2(b) is the ability to selectively couple all spin states within the V_{Si} qudit [36]. In particular, the $\Delta m_S = \pm 2$ transitions are normally forbidden for microwave-driven spin resonance. Therefore, their excitation in Fig. 2(b) represents a clear evidence of the acoustic nature of the observed resonances. To further corroborate this acoustic nature, we display in Fig. 2(c) the intensity of the optically detected $\Delta m_S = \pm 2$ SAR as a function of the magnetic field strength (vertical axis) and the rf frequency applied to the SAW resonator (horizontal axis). The SAR signal vanishes as soon as either B is changed or f_{SAW} is detuned (cf. S_{11} in the same panel), thus confirming that the spin transitions are caused by the dynamic fields of the SAW. Additional evidences for the acoustic nature are summarized in the SM [27].

We now discuss the anisotropic nature of the SAR. Figure 2(b) compares the optically detected SAR signal for two angles ϕ_B between the SAW propagation direction [x-axis, cf. Fig. 1(b)] and the in-plane magnetic field. While the magnetic field strengths at which the SARs take place are independent of the in-plane orientation of $\boldsymbol{B}$, the SAR intensities do clearly depend on ϕ_B. The full anisotropic behavior with respect to the field orientation on the sample plane is summarized by the circles in Fig. 3(c),(d), which display the intensity of the $\Delta m_S = \pm 1$ and $\Delta m_S = \pm 2$ SARs, respectively, as a function of ϕ_B.

To understand the unusual angular dependence of the SARs, we develop a microscopic model for the

spin-acoustic interaction. In the spherical approximation, the effect of a lattice deformation on a spin center is described by the interaction term

$$\mathcal{H}_{\mathrm{def}} = \Xi \sum_{\alpha\beta} u_{\alpha\beta} S_\alpha S_\beta, \tag{3}$$

where Ξ is the interaction constant [2]. Being quadratic in the spin operators, such an interaction can induce spin transitions with $\Delta m_S = \pm 1$ as well as with $\Delta m_S = \pm 2$. For $\boldsymbol{B} \| x$, the spin transitions with $\Delta m_S = \pm 1$ are induced by the strain tensor components u_{xy} and u_{xz}, while those with $\Delta m_S = \pm 2$ are induced by the other linear-independent components u_{yy}, u_{zz}, and u_{yz}. The strain components responsible for the spin transitions for other $\boldsymbol{B}$ directions can be obtained by the corresponding rotation of the strain tensor.

A plane Rayleigh SAW propagating along x [cf. Fig. 1(b)] is described by the strain tensor $u_{\alpha\beta}(t, x, z) = u_{\alpha\beta}(z) \mathrm{e}^{ikx - i\omega t} + \mathrm{c.c.}$ with nonvanishing components u_{xx}, u_{zz}, and $u_{xz} = \mathrm{i} u_{xz}''$ [37]. We assume a reference frame for which u_{xx}, u_{zz}, and u_{xz}'' are purely real. The factor $\mathrm{i} = \sqrt{-1}$ indicates that the phase of the u_{xz} component is shifted by $\pi/2$, thus resulting in an elliptically polarized strain field in the xz plane. Figure 2(d) displays the calculated depth profiles of the u_{xx}, u_{zz}, and u_{xz} strain components [38] superimposed on the simulated depth distribution of the V_{Si} defects [26].

In our case, the spin centers are inserted in an acoustic resonator and, thus, subjected to a combination of two counterpropagating SAWs traveling along x and $-x$ with intensities I_+ and I_-, respectively. We use the parameter $\eta = (I_+ - I_-)/(I_+ + I_-)$ to distinguish between a standing wave ($|\eta| = 0$), a traveling wave ($|\eta| = 1$), or intermediate cases ($0 < |\eta| < 1$). The rates $W_{\pm 1}$ and $W_{\pm 2}$ of the spin transitions with $\Delta m_S = \pm 1$ and $\Delta m_S = \pm 2$, respectively, are then given by (see SM [27])

$$\begin{aligned} W_{\pm 1} &\propto 3\cos^2\phi_B \langle u_{xx}^2 \sin^2\phi_B + u_{xz}''^2 + 2\eta u_{xx} u_{xz}'' \sin\phi_B \rangle \\ W_{\pm 2} &\propto \frac{3}{4} \langle (u_{xx}\sin^2\phi_B - u_{zz})^2 + 4u_{xz}''^2 \sin^2\phi_B \\ &\quad + 4\eta (u_{xx}\sin^2\phi_B - u_{zz}) u_{xz}'' \sin\phi_B \rangle. \end{aligned} \tag{4}$$

The transition rates in Eq. (4) were averaged along x to account for the finite size of the photoluminescence detection spot, which is larger than the SAW wavelength. The angular brackets $\langle\rangle$ indicate averaging along z to take into account the depth distribution of the V_{Si} centers as well as the strain field, as presented in Fig. 2(d).

Figures 3(a) and 3(b) present the angular dependencies of the $\Delta m_S = \pm 1$ and $\Delta m_S = \pm 2$ transition intensities, respectively, calculated after Eq. (4) for various η. The SARs are always symmetric with respect to the inversion of the B_x component, since our system has a (xz) mirror plane. For $\eta = 0$, the SARs are also symmetric with respect to the inversion of B_y due to additional presence of the time-reversal symmetry. As $|\eta|$ increases, the latter symmetry breaks as the strain field of the traveling SAW acquires an elliptical polarization. Particularly, Fig. 3(a) shows that the $\Delta m_S = \pm 1$ SAR almost vanishes for $B_y > 0$ ($0° < \phi_B < 180°$) while it remains strong for $B_y < 0$ ($180° < \phi_B < 360°$). Such an asymmetric angular dependence is a clear evidence of the broken time-reversal symmetry in the presence of a traveling SAW. Upon inversion of the SAW propagation direction ($\eta < 0$, not shown), the angular dependencies of such chiral SAR are flipped with respect to the horizontal axis.

Having developed a microscopic model for the anisotropic SAR, we now apply it to analyze the experimental data given by the circles in Fig. 3(c) and 3(d). The angular dependence of the $\Delta m_S = \pm 1$ SAR has a butterfly-like shape with vanishing signal for $\phi_B = \pm 90°$ and maxima when the magnetic field rotates toward $\phi_B \approx \pm 45°$ or $\pm 135°$. In contrast, the angular dependence of the $\Delta m_S = \pm 2$ SAR has a cocoon-like shape with maxima for $\phi_B = \pm 90°$. This SAR does not vanish for any direction of the in-plane magnetic field. The measured angular dependencies are best reproduced by Eq. (4) by assuming $\eta = 0$, which yields the solid lines in Fig. 3(c), (d). This result is consistent with the expected standing-wave nature of the acoustic fields within a resonator. We attribute the deviations between experimental data and theoretical predictions to small fluctuations in the position of the laser spot on the SAW path as the sample is rotated during the measurement [27]. We emphasize that our model has no fitting parameters except for the overall intensity to match the readout optical signal. Moreover, the absolute SAR intensities are comparable with those of conventional optically detected magnetic resonance induced by a microwave magnetic field with the amplitude $B_{\mathrm{rf}} \approx 30\ \mu\mathrm{T}$ [27]. This allows us to give a rough order of magnitude estimate for the spin-strain interaction constant, $\Xi \sim g\mu_B B_{\mathrm{rf}}/|u_{\alpha\beta}| \sim 10\ \mu\mathrm{eV}$. Its exact determination requires the measurement of the zero-field splitting as a function of the mechanical stress, which is beyond the scope of this work [39].

In conclusion, we demonstrate here half-integer SAR in SiC at room temperature. Using a SAW resonator patterned on the SiC surface, we are able to address both the $\Delta m_S = \pm 1$ and the $\Delta m_S = \pm 2$ spin transitions of the V_{Si} spin-3/2 center with all-optical readout and without requiring extra microwave electromagnetic fields. The SARs reveal a complex dependence on the magnetic field orientation with respect to the SAW propagation direction. Our theoretical model describes these angular dependencies without any fitting parameter, allows us to determine the spin-strain coupling constant, and predicts chiral spin-acoustic interaction for traveling SAWs. Such a room-temperature hybrid spin-mechanical platform can be used to implement quantum sensors [41] with on-chip SAW control instead of microwave electromagnetic fields [2] as

well as to realize acoustically driven topological states [42]. It can also be applied to implement microwave-free spin and optical control of single qubits in SiC [43–45].

The authors would like to thank S. Meister and S. Rauwerdink for technical support in the preparation of the samples, S. A. Tarasenko and M. Helm for discussions and critical questions, and S. Fölsch for a critical reading of the manuscript. A. V. P. acknowledges the support from the Russian Science Foundation (Project No. 20-42-04405) and the Foundation "BASIS." G. V. A. acknowledge the support from the German Research Foundation under Grant No. AS 310/5-1. Support from the Ion Beam Center at Helmholtz-Zentrum Dresden-Rossendorf is gratefully acknowledged for the proton irradiation.

*Corresponding author.
alberto.h.minguez@pdi-berlin.de

[1] M. J. A. Schuetz, E. M. Kessler, G. Giedke, L. M. K. Vandersypen, M. D. Lukin, and J. I. Cirac, Universal Quantum Transducers Based on Surface Acoustic Waves, Phys. Rev. X **5**, 031031 (2015).

[2] A. V. Poshakinskiy and G. V. Astakhov, Optically detected spin-mechanical resonance in silicon carbide membranes, Phys. Rev. B **100**, 094104 (2019).

[3] S. Kolkowitz, A. C. B. Jayich, Q. P. Unterreithmeier, S. D. Bennett, P. Rabl, J. G. E. Harris, and M. D. Lukin, Coherent sensing of a mechanical resonator with a single-spin qubit, Science **335**, 1603 (2012).

[4] S. Maity, L. Shao, S. Bogdanović, S. Meesala, Y.-I. Sohn, N. Sinclair, B. Pingault, M. Chalupnik, C. Chia, L. Zheng, K. Lai, and M. Lončar, Coherent acoustic control of a single silicon vacancy spin in diamond, Nat. Commun. **11**, 193 (2020).

[5] B. Machielse, S. Bogdanovic, S. Meesala, S. Gauthier, M. J. Burek, G. Joe, M. Chalupnik, Y. I. Sohn, J. Holzgrafe, R. E. Evans, C. Chia, H. Atikian, M. K. Bhaskar, D. D. Sukachev, L. Shao, S. Maity, M. D. Lukin, and M. Loncar, Quantum Interference of Electromechanically Stabilized Emitters in Nanophotonic Devices, Phys. Rev. X **9**, 031022 (2019).

[6] D. Lee, K. W. Lee, J. V. Cady, P. Ovartchaiyapong, and A. C. B. Jayich, Topical review: Spins and mechanics in diamond, J. Opt. **19**, 033001 (2017).

[7] K. J. Satzinger, Y. P. Zhong, H. S. Chang, G. A. Peairs, A. Bienfait, M.-H. Chou, A. Y. Cleland, C. R. Conner, É. Dumur, J. Grebel, I. Gutierrez, B. H. November, R. G. Povey, S. J. Whiteley, D. D. Awschalom, D. I. Schuster, and A. N. Cleland, Quantum control of surface acoustic-wave phonons, Nature (London) **563**, 661 (2018).

[8] S. Takada, H. Edlbauer, H. V. Lepage, J. Wang, P.-A. Mortemousque, G. Georgiou, C. H. W. Barnes, C. J. B. Ford, M. Yuan, P. V. Santos, X. Waintal, A. Ludwig, A. D. Wieck, M. Urdampilleta, T. Meunier, and C. Bäuerle, Sound-driven single-electron transfer in a circuit of coupled quantum rails, Nat. Commun. **10**, 4557 (2019).

[9] H. Zhu, J. Yi, M.-Y. Li, J. Xiao, L. Zhang, C.-W. Yang, R. A. Kaindl, L.-J. Li, Y. Wang, and X. Zhang, Observation of chiral phonons, Science **359**, 579 (2018).

[10] E. R. MacQuarrie, T. A. Gosavi, N. R. Jungwirth, S. A. Bhave, and G. D. Fuchs, Mechanical Spin Control of Nitrogen-Vacancy Centers in Diamond, Phys. Rev. Lett. **111**, 227602 (2013).

[11] O. Arcizet, V. Jacques, A. Siria, P. Poncharal, P. Vincent, and S. Seidelin, A single nitrogen-vacancy defect coupled to a nanomechanical oscillator, Nat. Phys. **7**, 879 (2011).

[12] J. Teissier, A. Barfuss, P. Appel, E. Neu, and P. Maletinsky, Strain Coupling of a Nitrogen-Vacancy Center Spin to a Diamond Mechanical Oscillator, Phys. Rev. Lett. **113**, 020503 (2014).

[13] D. A. Golter, T. Oo, M. Amezcua, K. A. Stewart, and H. Wang, Optomechanical Quantum Control of a Nitrogen-Vacancy Center in Diamond, Phys. Rev. Lett. **116**, 143602 (2016).

[14] H. Chen, N. F. Opondo, B. Jiang, E. R. MacQuarrie, R. S. Daveau, S. A. Bhave, and G. D. Fuchs, Engineering electron–phonon coupling of quantum defects to a semi-confocal acoustic resonator, Nano Lett. **19**, 7021 (2019).

[15] D. Riedel, F. Fuchs, H. Kraus, S. Väth, A. Sperlich, V. Dyakonov, A. A. Soltamova, P. G. Baranov, V. A. Ilyin, and G. V. Astakhov, Resonant Addressing and Manipulation of Silicon Vacancy Qubits in Silicon Carbide, Phys. Rev. Lett. **109**, 226402 (2012).

[16] A. L. Falk, B. B. Buckley, G. Calusine, W. F. Koehl, V. V. Dobrovitski, A. Politi, C. A. Zorman, P. X. L. Feng, and D. D. Awschalom, Polytype control of spin qubits in silicon carbide, Nat. Commun. **4**, 1819 (2013).

[17] M. Li, H. X. Tang, and M. L. Roukes, Ultra-sensitive NEMS-based cantilevers for sensing, scanned probe and very high-frequency applications, Nat. Nanotechnol. **2**, 114 (2007).

[18] A. L. Falk, P. V. Klimov, B. B. Buckley, V. Ivády, I. A. Abrikosov, G. Calusine, W. F. Koehl, A. Gali, and D. D. Awschalom, Electrically and Mechanically Tunable Electron Spins in Silicon Carbide Color Centers, Phys. Rev. Lett. **112**, 187601 (2014).

[19] S. J. Whiteley, G. Wolfowicz, C. P. Anderson, A. Bourassa, H. Ma, M. Ye, G. Koolstra, K. J. Satzinger, M. V. Holt, F. J. Heremans, A. N. Cleland, D. I. Schuster, G. Galli, and D. D. Awschalom, Spin–phonon interactions in silicon carbide addressed by Gaussian acoustics, Nat. Phys. **15**, 490 (2019).

[20] H. Kraus, V. A. Soltamov, D. Riedel, S. Väth, F. Fuchs, A. Sperlich, P. G. Baranov, V. Dyakonov, and G. V. Astakhov, Room-temperature quantum microwave emitters based on spin defects in silicon carbide, Nat. Phys. **10**, 157 (2014).

[21] V. A. Soltamov, C. Kasper, A. V. Poshakinskiy, A. N. Anisimov, E. N. Mokhov, A. Sperlich, S. A. Tarasenko, P. G. Baranov, G. V. Astakhov, and V. Dyakonov, Excitation and coherent control of spin qudit modes in silicon carbide at room temperature, Nat. Commun. **10**, 1678 (2019).

[22] P. Udvarhelyi and A. Gali, Ab Initio Spin-Strain Coupling Parameters of Divacancy Qubits in Silicon Carbide, Phys. Rev. Applied **10**, 054010 (2018).

[23] V. Ivády, J. Davidsson, N. T. Son, T. Ohshima, I. A. Abrikosov, and A. Gali, Identification of Si-vacancy related room-temperature qubits in 4H silicon carbide, Phys. Rev. B **96**, 161114(R) (2017).

[24] H. Kraus, D. Simin, C. Kasper, Y. Suda, S. Kawabata, W. Kada, T. Honda, Y. Hijikata, T. Ohshima, V. Dyakonov, and

G. V. Astakhov, Three-dimensional proton beam writing of optically active coherent vacancy spins in silicon carbide, Nano Lett. **17**, 2865 (2017).

[25] The depth distribution was determined using SRIM (stopping and range of ions in matter) simulation [26].

[26] J. F. Ziegler, M. D. Ziegler, and J. P. Biersack, SRIM—The stopping and range of ions in matter, Nucl. Instrum. Methods Phys. Res., Sect. B **268**, 1818 (2010).

[27] See Supplemental Material at http://link.aps.org/supplemental/10.1103/PhysRevLett.125.107702 for sample and experimental details, photoluminescence characterization, optically detected magnetic resonance spectrum at zero magnetic field, spatial dependence of the SAR, dependence of the SAR on SAW power, and determination of the matrix elements for the SAW-induced spin transition.

[28] E. Sörman, N. T. Son, W. M. Chen, O. Kordina, C. Hallin, and E. Janzén, Silicon vacancy related defect in 4H and 6H SiC, Phys. Rev. B **61**, 2613 (2000).

[29] H. J. von Bardeleben, J. L. Cantin, L. Henry, and M. F. Barthe, Vacancy defects in p-type 6H − SiC created by low-energy electron irradiation, Phys. Rev. B **62**, 10841 (2000).

[30] S. B. Orlinski, J. Schmidt, E. N. Mokhov, and P. G. Baranov, Silicon and carbon vacancies in neutron-irradiated SiC: A high-field electron paramagnetic resonance study, Phys. Rev. B **67**, 125207 (2003).

[31] S. A. Tarasenko, A. V. Poshakinskiy, D. Simin, V. A. Soltamov, E. N. Mokhov, P. G. Baranov, V. Dyakonov, and G. V. Astakhov, Spin and optical properties of silicon vacancies in silicon carbide—A review, Phys. Status Solidi (b) **255**, 1700258 (2018).

[32] These dips appear at the frequencies for which the effective length of the SAW cavity is a multiple integer of $\lambda_{\mathrm{SAW}}/2$.

[33] V. A. Soltamov, B. V. Yavkin, D. O. Tolmachev, R. A. Babunts, A. G. Badalyan, V. Y. Davydov, E. N. Mokhov, I. I. Proskuryakov, S. B. Orlinskii, and P. G. Baranov, Optically Addressable Silicon Vacancy-Related Spin Centers in Rhombic Silicon Carbide with High Breakdown Characteristics and ENDOR Evidence of Their Structure, Phys. Rev. Lett. **115**, 247602 (2015).

[34] D. Simin, V. A. Soltamov, A. V. Poshakinskiy, A. N. Anisimov, R. A. Babunts, D. O. Tolmachev, E. N. Mokhov, M. Trupke, S. A. Tarasenko, A. Sperlich, P. G. Baranov, V. Dyakonov, and G. V. Astakhov, All-Optical dc Nanotesla Magnetometry Using Silicon Vacancy Fine Structure in Isotopically Purified Silicon Carbide, Phys. Rev. X **6**, 031014 (2016).

[35] C. Kasper, D. Klenkert, Z. Shang, D. Simin, A. Gottscholl, A. Sperlich, H. Kraus, C. Schneider, S. Zhou, M. Trupke, W. Kada, T. Ohshima, V. Dyakonov, and G. V. Astakhov, Influence of Irradiation on Defect Spin Coherence in Silicon Carbide, Phys. Rev. Applied **13**, 044054 (2020).

[36] In large magnetic fields considered here, the spin-acoustic interaction does not couple the $m_S = -3/2$ and $m_S = +3/2$ states. In case of $\boldsymbol{B} \sim D/\mu_B$, any pair within the four spin states can be coupled acoustically.

[37] L. Rayleigh, On waves propagated along the plane surface of an elastic solid, Proc. London Math. Soc. **s1-17**, 4 (1885).

[38] M. M. de Lima, Jr. and P. V. Santos, Modulation of photonic structures by surface acoustic waves, Rep. Prog. Phys. **68**, 1639 (2005).

[39] The obtained value of Ξ is 2 orders of magnitude smaller than that supposed in Ref. [2]. This indicates that the contribution of the spin-acoustic interaction of the form Eq. (3) to the spin-lattice relaxation rate is not dominant. On the other hand, the obtained value of Ξ agrees well with the recent experimental results on stress-induced spatial variation of the spin transition energies in centers located near a heterointerface [40].

[40] I. D. Breev, A. V. Poshakisnkiy, E. N. Mokhov, P. G. Baranov, and A. N. Anisimov, Effect of mechanical stress on fine structure of spin centers in silicon carbide (to be published).

[41] H. Kraus, V. A. Soltamov, F. Fuchs, D. Simin, A. Sperlich, P. G. Baranov, G. V. Astakhov, and V. Dyakonov, Magnetic field and temperature sensing with atomic-scale spin defects in silicon carbide, Sci. Rep. **4**, 5303 (2014).

[42] L. Zhang and Q. Niu, Chiral Phonons at High-Symmetry Points in Monolayer Hexagonal Lattices, Phys. Rev. Lett. **115**, 115502 (2015).

[43] R. Nagy, M. Niethammer, M. Widmann, Y.-C. Chen, P. Udvarhelyi, C. Bonato, J. u. Hassan, R. Karhu, I. G. Ivanov, N. T. Son, J. R. Maze, T. Ohshima, Ö. O. Soykal, A. Gali, S.-Y. Lee, F. Kaiser, and J. Wrachtrup, High-fidelity spin and optical control of single silicon-vacancy centres in silicon carbide, Nat. Commun. **10**, 1954 (2019).

[44] D. M. Lukin, C. Dory, M. A. Guidry, K. Y. Yang, S. D. Mishra, R. Trivedi, M. Radulaski, S. Sun, D. Vercruysse, G. H. Ahn, and J. Vučković, 4H-silicon-carbide-on-insulator for integrated quantum and nonlinear photonics, Nat. Photonics **14**, 330 (2020).

[45] B. Machielse, S. Bogdanovic, S. Meesala, S. Gauthier, M. J. Burek, G. Joe, M. Chalupnik, Y. I. Sohn, J. Holzgrafe, R. E. Evans, C. Chia, H. Atikian, M. K. Bhaskar, D. D. Sukachev, L. Shao, S. Maity, M. D. Lukin, and M. Lončar, Quantum Interference of Electromechanically Stabilized Emitters in Nanophotonic Devices, Phys. Rev. X **9**, 031022 (2019).